catalysts

Article

Activity of Catalytic Ceramic Papers to Remove Soot Particles—A Study of Different Types of Soot

Sabrina Antonela Leonardi, Eduardo Ernesto Miró and Viviana Guadalupe Milt *

Instituto de Investigaciones en Catálisis y Petroquímica, INCAPE (FIQ, UNL-CONICET),
Santiago del Estero 2829, Santa Fe 3000, Argentina; sleonardi@fiq.unl.edu.ar (S.A.L.);
emiro@fiq.unl.edu.ar (E.E.M.)
* Correspondence: vmilt@fiq.unl.edu.ar

Abstract: Diesel soot particles are of concern for both the environment and health. To catalytically remove them, it is important to know their structure and composition. There is little described in the literature on how catalysts favor the combustion of different soot fractions. In this work, programmed temperature oxidation (TPO) experiments were carried out using Co,Ce or Co,Ba,K catalysts supported on ceramic papers. Soot particles were obtained by burning diesel fuel in a vessel (LabSoot) or by filtering exhaust gases from a turbo diesel engine in a DPF filter (BenchSoot), and compared with a commercial diesel soot: Printex U. Various characterization techniques were useful to relate the characteristics of both the soot particles and the catalysts with the TPO results. The maximum catalytic soot burn rate (T_M) temperatures were in the range of diesel exhaust temperatures that would facilitate in-situ regeneration of the DPF. The Co,Ba,K catalyst showed a higher catalytic effect in LabSoot, as the latter exhibited the largest primary particles and the higher order of graphene layers, for which the potassium-containing catalyst improves the contact between soot and catalyst and favors the combustion of soot, while the Co,Ce catalyst preferentially enhanced the combustion of commercial soot by supplying active oxygen.

Keywords: diesel soot reactivity; laboratory soot; bench-collected soot; ceramic paper catalysts; Co,Ce catalyst; Co,Ba,K catalyst

check for updates

Citation: Leonardi, S.A.; Miró, E.E.; Milt, V.G. Activity of Catalytic Ceramic Papers to Remove Soot Particles—A Study of Different Types of Soot. *Catalysts* **2022**, *12*, 855. https://doi.org/10.3390/catal12080855

Academic Editor: Pedro B. Tavares

Received: 14 July 2022
Accepted: 30 July 2022
Published: 3 August 2022

1. Introduction

Soot particles emitted by modern diesel engines, despite having a significantly lower total mass, exhibit higher reactivity and toxicity than older black smoke engines, leading to serious health and environmental problems [1]. In fact, ultrafine soot particles (UFP, <100 nm) can enter the human body more easily and deeply, being more dangerous than larger ones [2]. Among the contaminants emitted by diesel engines (CO, NOx, unburned hydrocarbons and soot), carbonaceous particles are probably the most difficult to control.

Soot emission is linked to partial oxidation of diesel fuel and is produced in the hot, fuel-rich reaction zone surrounding individual fuel droplets, where fuel hydrocarbons are oxidized under oxygen deficiency [3,4]. The very small atomized fuel droplets burn in the hot compressed air forming aggregates of carbon nanoparticles with adsorbed hydrocarbons [5]. These agglomerates constitute the so-called "particulate matter" (PM), the carbonaceous part of which has an onion-shaped graphene sheet structure [6].

Soot removal requires active species supported on a structure, in order to simultaneously retain and remove soot while the diesel vehicle is running [7]. The most common way of trapping diesel soot is the use of catalytic diesel particulate filters (CDPF) that employ surface filtration, sometimes referred to as cake filtration or sieving [8], using cordierite [9] or silicon carbide monoliths [10]. Nonetheless, usually, these monoliths offer a considerable pressure drop and have narrow channel structures in their interior, where laminar flows occur, and this fact implies a limitation of mass transfer from the gas phase to the catalytic layer of the wall [11].

A second approach is to use deep-bed filters with fairly open-structured materials compared to surface filters, such as foams [12] or metal meshes [11]. In these filters, soot is retained throughout the filter structure by three well-established mechanisms: inertial and flowline intercepts and Brownian diffusion [8]. The main benefit of this arrangement is that the contact between the deposited soot and the catalytic coating of the filter is much better, which facilitates the continuous regeneration of the filter. Another possible configuration is using a similar structure to that of conventional paper but made of ceramic fibers instead of cellulosic ones.

Ceramic papers consist of a fibrous matrix with porous-type spaces that facilitate the diffusion of gases [13]. The use of ceramic fibers in the paper manufacturing process provides, after calcination, ceramic papers that withstand temperatures above 900 °C [14]. Several methods have been used for the deposition of catalysts on ceramic papers, such as wet impregnation [15], wet spraying [16] and dry spraying [17]. Catalytic papers offer an attractive alternative for the development of systems that can simultaneously act as a particulate filter and as a structured catalyst with self-regeneration capability (passive regeneration) [18].

Several works have been published about the oxidation reactivity of different types of carbonaceous particles but most of them under non-catalyzed conditions [19–23]. In a pioneer work, Medalia et al. [24] examined six types of carbon black and eighteen samples of soot. They observed that carbon black is formed by turbo-stratic colloidal aggregates called aciniform carbon (AC) and that diesel soot consisted mainly of AC and SOF (soluble organic fraction), SOF being especially important since it contains carcinogenic compounds which confer carcinogenic activity to soot. In addition, all of the soot samples examined contained much larger amounts of ash than carbon black.

Many years later, Meng et al. [25] compared the non-catalytic combustion of a model carbon black (Printex U) with that of diesel soot. They found that diesel-soot combustion occurred through two steps. The first one at lower temperatures, owing to the presence of disordered carbon and the soluble organic fraction (SOF), and the second one at higher temperatures, originating from carbon black combustion. They concluded that, compared to carbon black and under identical conditions, diesel soot oxidized more easily because of its lower ignition temperature.

Recently, Zhang et al. [1] reported an investigation of nanostructures of diesel soot sampled from diesel flames and exhaust stream from a running engine. Their findings revealed that comparable multiple cores made up of short graphene segments and an external cover consisting of widespread sheets of graphitic carbon were observed both for soot particles coming from the flame and from diesel burning. On the other hand, Lee et al. [2] synthesized diesel soot by controlling the particle size and the amount of organic matter and concluded that the oxidation reactivity is influenced by the nanostructure and the degree of carbonization.

Many formulations of active catalysts have been studied and reported for soot combustion, which can be assisted by both NO_2 and active oxygen in the catalyst, even when the contact between soot and catalyst is loose. These catalysts can be classified as noble metals, single and mixed oxides and molten salts. Among them, ceria has been widely studied since it is able to generate and transport active oxygen to the surface of the catalyst, even under loose contact conditions [26]. The importance of the redox properties of these oxides that help replacing surface oxygen increasing soot oxidation activity is widely recognized. In addition, the combination of ceria with different elements, such as manganese, has become a topic of great interest in recent years [27].

Most of the activity and stability studies have been conducted using powder formulations and model soot particles such as commercial Printex U [28]. However, the soot–catalyst contact during the filtration and regeneration of the catalytic filter is different from that obtained with powder catalysts, so although valuable information regarding intrinsic activity is obtained with the latter, these results cannot be directly extended to CDPFs [29]. In our group, we have chosen to use synthetic soot obtained by the combustion of commercial diesel fuel (YPF, Argentina) [30]. However, although being a better approach to real soot than Printex U, we are aware of possible differences existing in the conditions under which real diesel soot is formed inside the engine cylinder.

Scarce information is found in the open literature concerning the oxidation reactivity of different types of carbonaceous particles under catalyzed conditions. Even less is found using structured catalysts, which can be extended to CDPFs. An interesting article has recently been published that deals with the use of a structured diesel-soot oxidation catalyst coupled to a catalytic particulate filter (DOC-CDPF assembly) using cordierite monoliths loaded with noble metals, where the effect of soot composition was studied under different regimes of the engine along the components of the exhaust aftertreatment system [31]. An important conclusion drawn was that the catalyst constituents in the aftertreatment systems effectively augment the graphitization of exhaust particles, producing more stable particles that would need higher energies of active regeneration or more active catalysts on the surface of the CDPF wall to clean them up.

In this work, we study two different types of soot samples and their catalytic combustion using catalytic ceramic papers developed in previous works [17,32], in order to investigate the effect of their properties on the reactivity of soot towards combustion in the presence of oxygen and NOx.

Ceramic papers consist of a matrix of SiO_2-Al_2O_3 fibers joined by CeO_2 nanoparticles as binder and Co,Ce or Co,Ba,K as active phases. These catalysts combine ceria oxygen storage and the mobility and redox properties of cobalt. For Co,Ba,K, barium acts as an NO trap and the presence of potassium enhances soot-to-catalyst contact. Moreover, these catalysts showed high activity and stability performances [32], suitable to simulate the passive regeneration of the CDPF. Additionally, ceramic-paper catalysts are flexible structures that can be easily adapted to different configurations in view of the potential practical application of these systems.

One of the soot samples studied was collected after burning diesel fuel in a vessel at a lab scale, and the other one from the filtration of the exhausts of a bench diesel engine. In the second case, a metal cartridge filled with catalytic ceramic paper was used as CDPF. Printex U was also employed for comparison purposes. Soot samples were characterized using transmission electron microscopy (HR-TEM), laser raman spectroscopy (LRS), X-ray fluorescence spectroscopy (XRF), infrared spectroscopy (FTIR), scanning differential thermal analysis (SDTA) and thermogravimetric analysis (TGA) to gain insight into the structure and chemical aspects of the soot. The activity of catalytic ceramic papers was evaluated through TPO experiments. Although the catalytic papers were already characterized in terms of physical chemistry properties [17,32], in this work, we include their morphological characterization by means of X-ray tomography and scanning electron microscopy (SEM), permeation studies, and determination of mechanical properties.

2. Results and Discussion

2.1. Soot Characterization

Figure 1a shows TGA profiles obtained when heating the different types of diesel soot under air flow, i.e., the Printex U soot model, the one obtained from burnt diesel fuel (LabSoot) and that collected from the exhausts of a bench diesel engine (BenchSoot). LabSoot loses about 93 wt.% mass between 420 and 550 °C, as seen in the corresponding TGA profile, accompanied by an exothermic heat evolution shown in the SDTA profile (Figure 1b), as indicated by the peak with a maximum at 525 °C. This last temperature is associated with the non-catalytic combustion of soot (carbonaceous fraction), remaining 4.5 wt.% ash after the heating up to 600 °C (Figure 1a). By XRF analysis, the ash chemical composition was found to be around 50 wt.% Fe, the other 50 wt.% being composed of Ca, S, K, Zr, Zn and Cu.

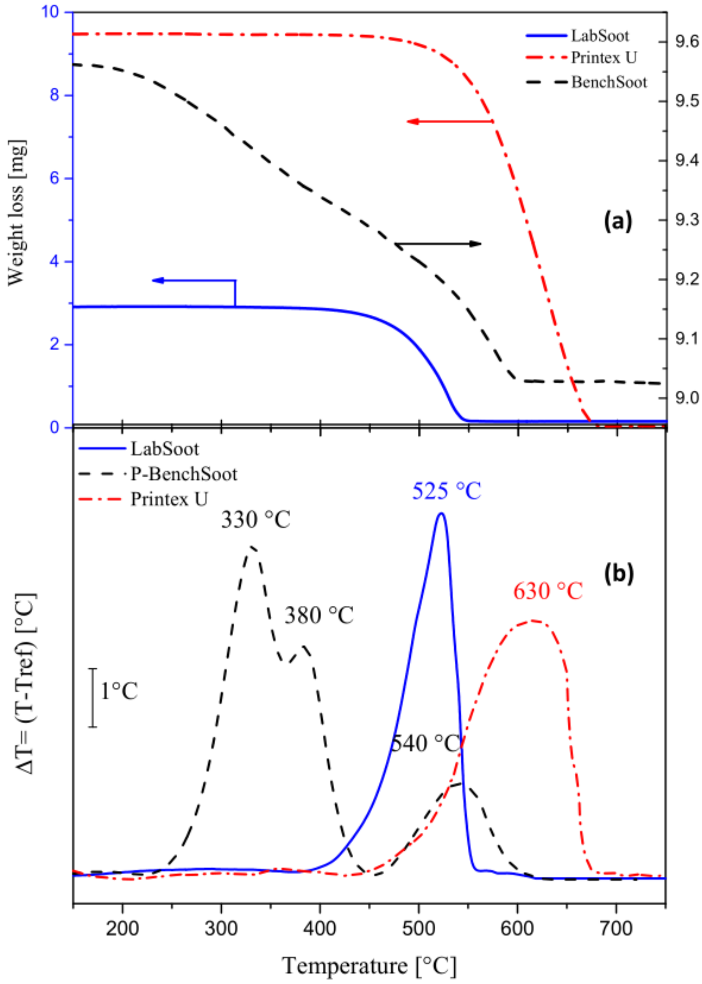

Figure 1. Thermogravimetric analyses: (**a**) TGA and (**b**) SDTA of bare LabSoot, bare Printex U and BenchSoot loaded on ceramic paper.

For BenchSoot, two zones of weight loss can be distinguished in the TGA profile (Figure 1a), characterized by small differences in their slopes: the first one between 185 and 450 °C and the second one between 500 and 600 °C. The zone at the lower temperature involves two exothermic evolutions that have maxima at 330 °C and 380 °C, whereas the other one at a high temperature shows a peak at 540 °C (exothermic evolution), shown in the respective SDTA curve (Figure 1b). The low-temperature peaks probably originated from the combustion of unburned hydrocarbons (HC adsorbed and/or condensed on soot), abundant in engine exhausts, which were also observed in a previous work [16]. The high-temperature peak is associated with the non-catalytic combustion of soot (carbonaceous fraction). However, after heating up to 600 °C, 94.7 wt.% weight remains. This percentage involves both the ash content and the ceramic paper weight, as it was not possible to separate soot particles from the filtering media (ceramic paper) for BenchSoot. By XRF analysis, the ash chemical composition was found to be at around 50 wt.% Fe, and the other 50 wt.% corresponded to Ca, S, K, Zr, Zn, Cu and Mn (values calculated without considering the amounts of SiO_2 and Al_2O_3 that compose the ceramic paper disc).

The composition of the ash varies for different types of soot owing to the presence of several classes of metallic compounds (containing P, S, Ca, Zn, Mg, and possible Na [33]) coming from additives added to lubricants, trace elements present in the fuel, and products generated by engine wear and corrosion. Nevertheless, as seen by XRF, no significant differences can be observed between the ash composition of LabSoot and BenchSoot, unless the presence of Mn in BenchSoot probably comes from lubricant oils.

On the other hand, the model soot sample (Printex U) is completely gasified between 450 and 670 °C, as observed in the corresponding TGA profile (Figure 1a), so that no ash was detected after combustion. The mass loss observed correlates to an exothermic evolution at 630 °C, indicated in the SDTA profile of Printex U (Figure 1b). In addition, the absence of peaks at lower temperatures would indicate the absence of adsorbed or condensed hydrocarbons.

To deepen this study, the soot samples were also characterized by infrared spectroscopy (Figure 2). The assignment of signals according to the type of groups adsorbed on LabSoot, BenchSoot, and Printex U samples is shown in the respective spectra. The spectrum corresponding to the BenchSoot sample shows signals between 2960 and 2850 cm^{-1} ascribed to the asymmetric and symmetric stretching vibrations of the C-H bond of both methyl and methylene species (CH_3, CH_2). Correspondingly, signals at 1384 and 1458 cm^{-1} associated to the C-H bond deformation vibrations of these groups are observed. These signals probably come from aliphatic hydrocarbons [34,35]. A broad signal appears at 1620 cm^{-1}, indicating the presence of an aromatic C=C bond [36]. The signals at 1040 and 1110 cm^{-1} are due to the stretching of C-O bonds of C-OH, C-O-C, and C-O groups, corresponding to functional groups of alcohols, ethers, and esters, respectively [36,37]. These signals are in line with the peaks observed at low temperatures for BenchSoot (330 and 380 °C) in the SDTA experiment (Figure 1b) and they are probably associated with unburnt hydrocarbons adsorbed and condensed on this sample.

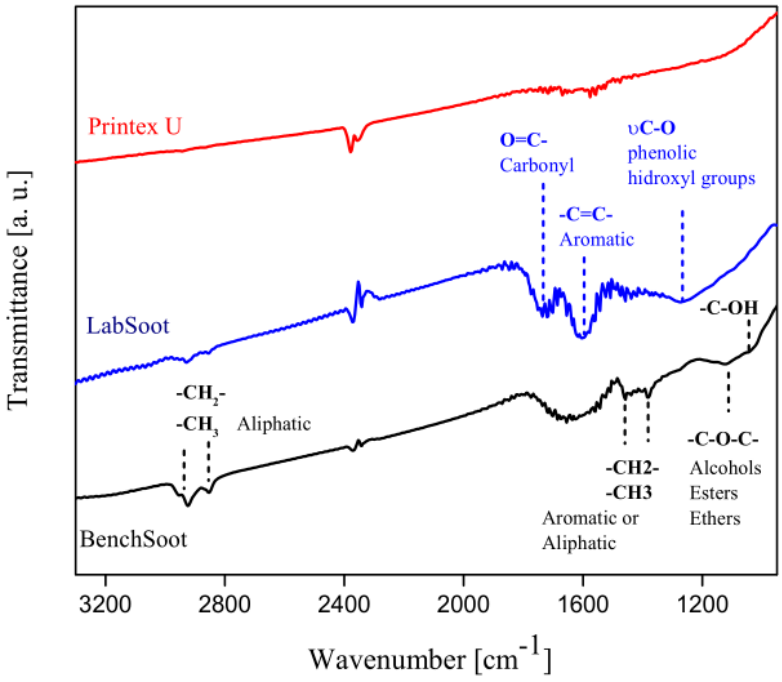

Figure 2. Infrared spectra of soot samples.

For LabSoot, similarly to that observed for BenchSoot, the signal of a C=C aromatic at 1620 cm^{-1} is clearly observed, whereas a signal observed at ca. 1740 cm^{-1} indicates the presence of carbonyl groups [34]. The lower intensities observed for aliphatic HC in the spectrum of LabSoot are associated to the higher temperature treatment at which the diesel fuel was exposed to produce the artificial soot. In fact, the FTIR technique allowed the identification of surface species, not detected during thermogravimetric analysis (Figure 1b).

The FTIR spectrum for the Printex U sample indicates the absence of condensed hydrocarbons, also evidenced by the absence of mass loss observed at low temperatures in TGA experiments (Figure 1a). Only low-intensity signals coming from atmospheric CO_2 (ca. 2200 cm^{-1}) and rotovibrational signals of water (ca. 1600 cm^{-1}) are seen in the spectrum.

The presence of surface oxygenated groups provides a fast soot-oxidation pathway. Song et al. [38], based on a previous contribution of Ishiguro et al. [39], used the ratio between intensity peaks at 1740 cm^{-1} (attributed to the stretching of the C=O groups from carboxylic acids, lactones and ketones) to that at 1620 cm^{-1} (corresponding to the stretching of the C=C bond of C=O conjugated aromatic systems), I_{1740}/I_{1620}, to estimate the relative abundance of superficial oxygen. This ratio could be estimated for LabSoot (I_{1740}/I_{1620} = 0.91) and for BenchSoot (I_{1740}/I_{1620} = 0.44), whereas in the case of Printex U, these peaks at 1740 and1620 cm^{-1} are not detected in the IR spectrum. This suggests the following order according to the content of surface oxygenated species: LabSoot > BenchSoot > Printex U.

According to TGA, SDTA and FTIR results for the BenchSoot sample, the SDTA peaks at 330 and 380 °C correspond to the combustion of different types of organic compounds, such as aliphatic, aromatic and oxygenated hydrocarbons, condensed on the carbonaceous core of soot particulates, whereas the high temperature peak (540 °C) corresponds to the combustion of the carbonaceous nuclei. In the case of LabSoot, the burning of the carbonaceous core appears at lower temperatures (525 °C), which could be associated with the higher content of oxygenated species (Figure 2). As these oxygenated species are superficial, no detectable exothermic peaks associated to their decomposition are observed in TGA experiments.

Raman spectroscopy is a powerful method to characterize carbon materials, since it is very sensitive to the short range disorder of carbon. The carbon materials are integrated with the linear chain of C-C atoms forming the monomers and polymers and can undergo different structural changes due to the rearrangement of the atoms through different hybridization. The existence of π-states in carbon materials with the sp^2 bonds have very long-range polarizability, leading to a large Raman cross section, making Raman spectroscopy a suitable choice [40].

Graphite is the stacked sheet of carbon atoms in the basal planes arranged in the sp^2 tetragonal configuration with weak interaction between the layers. It has two-dimensional hexagonal shapes with the fourth electron in the π-orbital and perpendicular to the weakly bonded hexagon sheets [41]. The graphitic structure has a high degree of disorder due to strong C-C bonding.

Accordingly, the different classes of soot were further analyzed utilizing LRS and Figure 3 displays the resulting spectra, composed of the G-peak, which relates to the graphitic-like structures and is originated from the doubly degenerated vibrational mode E_{2g} at about 1580 cm^{-1} and the D-peak at around 1360 cm^{-1} related to the disorder induced in the graphite and linked to A_{1g} symmetry. Both the ratio of amorphous to graphitic carbon and the degree of the ordering of the graphene layer were calculated by the deconvolution of the spectra to relate them to the reactivity of soot in the TPO runs. To this end, every Raman spectrum was fitted considering the contributions listed in Table 1, as proposed by Sadezky et al. [42].

Table 1. Raman signal contributions for the different samples of soot.

Band	Raman Shift (cm^{-1})	LabSoot Area	BenchSoot Area	Printex U Area	Vibration Mode
G	1580	18,612	4800	5800	Ideal graphitic lattice (E_{2g} symmetry)
D1	1372	31,855	11,500	11,500	Disordered graphitic lattice (A_{1g} symmetry)
D2	1616	4186	1300	1500	Disordered graphitic lattice (E_{2g} symmetry)
D3	1490	4490	4000	4800	Amorphous carbon
D4	1279	15,300	2500	3500	Disordered graphitic lattice (A_{1g} symmetry)

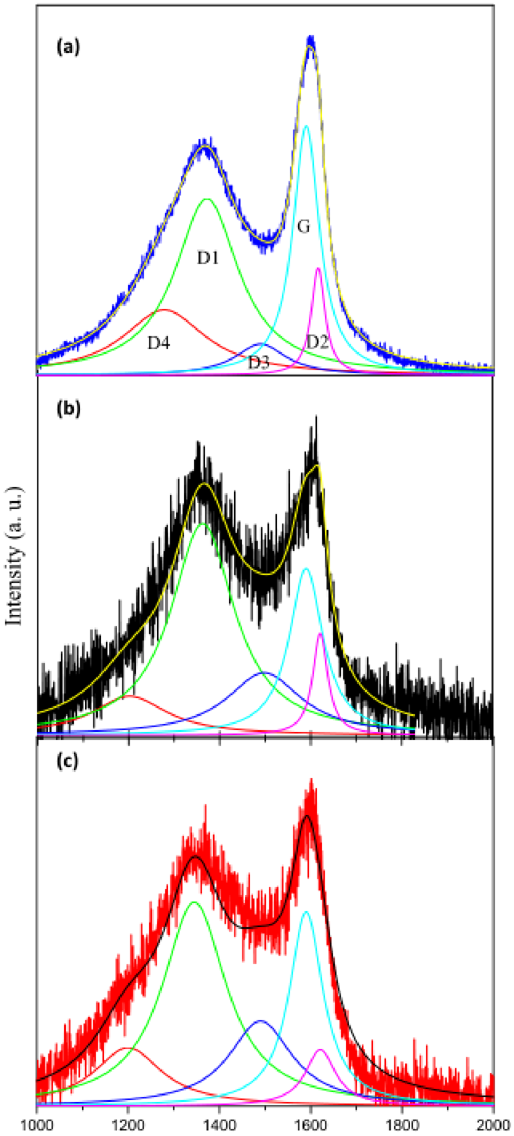

Figure 3. Laser Raman spectra of soot samples: (**a**) LabSoot [30], (**b**) BenchSoot, and (**c**) Printex U. Bands: G (cyan), D1 (green), D2 (pink), D3 (blue) and D4 (red).

The graphitic carbon content, expressed as a percentage, was obtained according to Equation (1) [30]:

$$\%\,\mathrm{GC} = \frac{100 \cdot I_G}{I_T} \tag{1}$$

in which % GC is the percentage of graphitic carbon and I_G and I_T are the corresponding areas of G peak and that of the sum of all the areas of the different peaks obtained from fitting the spectra, respectively. The resulting percent graphitic carbon content was 30.6%, 21.4%, and 19.9% for LabSoot, Printex U and BenchSoot, respectively (Table 2).

Table 2. Graphitic and amorphous contents and disorder degree for the different samples of soot.

Sample/Type of Carbon	LabSoot	BenchSoot	Printex U
Graphitic carbon percentage, %GC	30.6	19.9	21.4
Amorphous carbon percentage, %AC	6.0	16.6	17.7
I_{D1}/I_G	1.7	2.4	2.0

On the other hand, the percentage of amorphous carbon (% AC) was calculated according to Equation (2):

$$\% \text{ AC} = \frac{100 \cdot I_{D3}}{I_T} \quad (2)$$

where I_{D3} is the intensity (peak area) of the D3 peak that correlates with the amount of amorphous carbon. Table 2 lists amorphous carbon contents, which were similar for Printex U and BenchSoot samples, with values of 17.7% and 16.6%, respectively, whereas a lower value (6.0%) was observed for LabSoot. This type of carbon is easier to burn than graphitic carbon, which will influence TPO assays [43].

In addition, the I_{D1}/I_G ratio, where I_{D1} is the intensity of the D1 peak related to the disordered graphitic lattice, is indicative of the degree of graphene layers disordering, which increases with the value of I_{D1}/I_G. In this sense, values shown in Table 2 indicate higher disordering for BenchSoot and, consequently, the following order can be established according to the degree of graphitization: LabSoot > Printex U > BenchSoot.

On the other hand, the internal structure and morphological aspects of soot samples, such as size distribution, particle shape and the orientation of the graphene layer, were studied by TEM. The images obtained (Figure 4) show that particle size and agglomeration are different, depending on the method of obtaining soot samples. As Figure 4 shows, BenchSoot primary particles have an irregular shape with distribution sizes between 8 to 57 nm, and a compact agglomeration. In contrast, Printex U primary particles, with distribution sizes between 24 to 70 nm, have a spherical geometry and a chain-like agglomeration, as LabSoot particles do. However, the latter are the largest particles, between 48 to 154 nm, and oval in shape. From Figure 4 (bottom), the size order of mean primary particle size is BenchSoot < Printex U < LabSoot, with values of 23.8 nm, 47.5 nm and 102.5 nm, respectively.

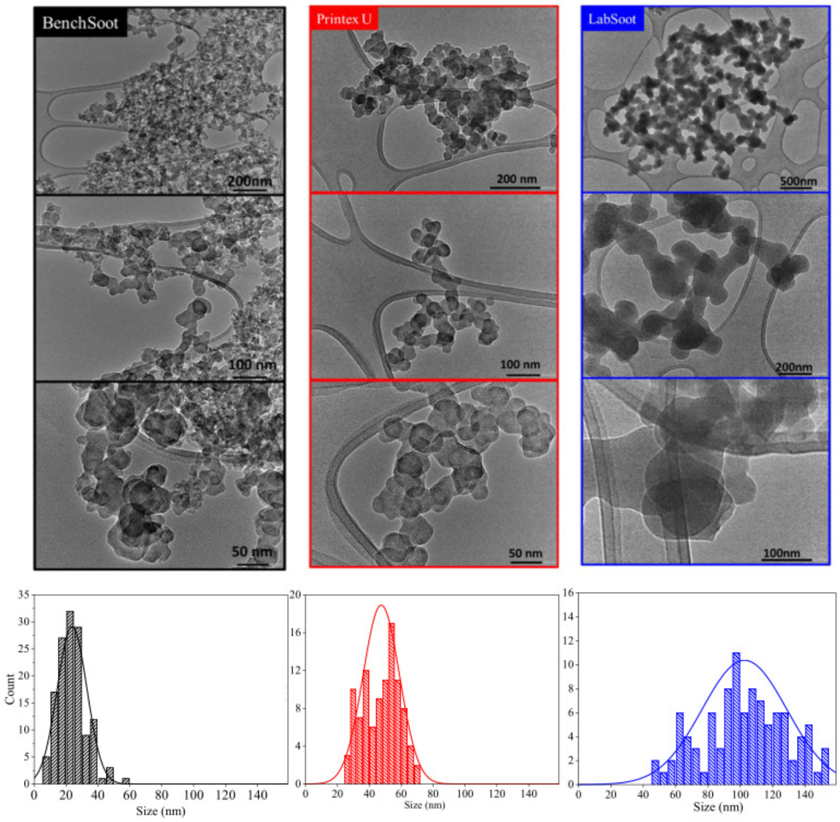

Figure 4. Soot nanostructure images using a high-resolution TEM and particle size distribution (bottom graphs).

In a detailed view (Figure 5), the orientation of the graphene layers for the different primary soot particles can be observed, consisting of an outer shell, related to graphitic carbon, and an inner core, related to amorphous carbon. The LabSoot sample shows a more defined orientation of the graphene layers with a small inner core, while for the Printex U and Bench Soot samples, the graphene layers acquire a certain degree of disorder and the size of the inner cores increases, which agrees with the results shown in Table 2 obtained from LR spectra. That is, the ratio of amorphous to graphitic carbon increases in the order LabSoot < Printex U < BenchSoot and, on the contrary, the degree of graphitization follows the order LabSoot > Printex U > BenchSoot.

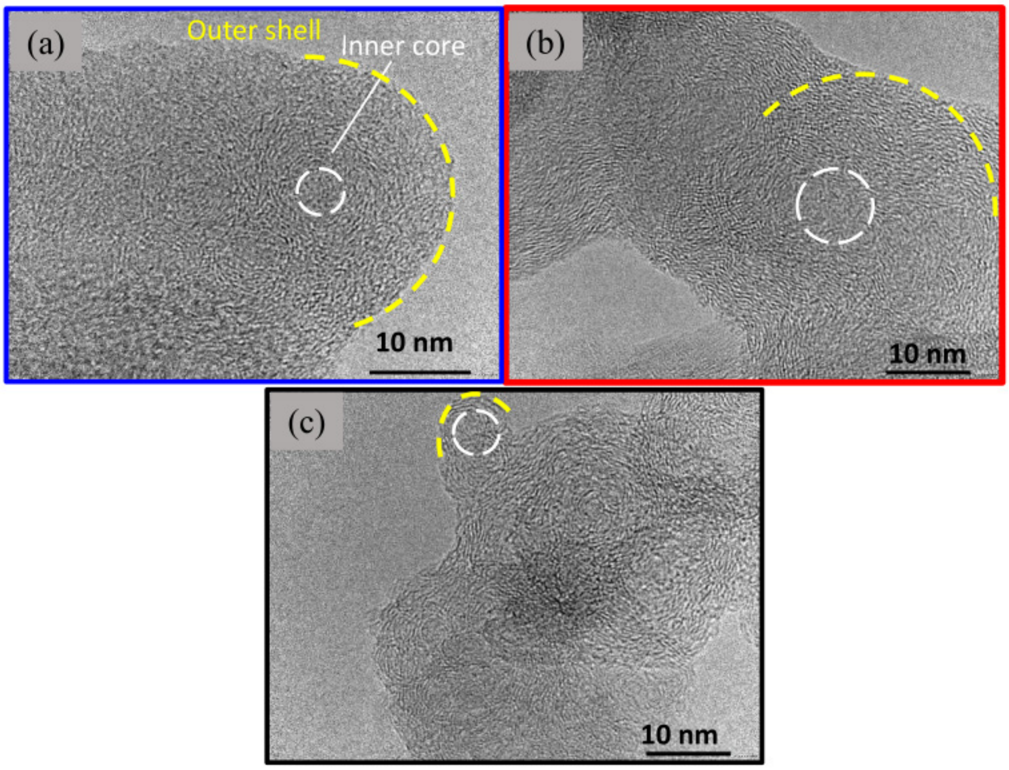

Figure 5. TEM images of primary particles (**a**) LabSoot, (**b**) Printex U and (**c**) BenchSoot samples.

It is noteworthy that both the soot particle agglomeration and the higher graphene layer disorder observed for the BenchSoot sample are similar to those found in vehicle soot particles [43], and are consistent with the higher amount of adsorbed hydrocarbons or oxygenated species found by TGA/SDTA and FTIR, with the more disordered soot structure being easier to burn.

2.2. Description of the Structured Catalyst

2.2.1. Ceramic Paper Discs

Figure 6 shows images of ceramic papers prepared as 160 mm diameter and 2.5 mm thick discs (Figure 6a,b). The flexibility of the structure can be appreciated in Figure 6c whereas Figure 6d shows how 160 mm ceramic discs can be cut into pieces in an easy way. Ceramic papers are composed of high-temperature-resistant ceramic fibers (up to 900 °C), which are cylindrical, 660 μm long and 6 μm in diameter. The intertwining of these fibers (SEM image, Figure 6e) provides a tortuous structure throughout the thickness of the disc that allows the soot particles to be retained. The latter, together with the arrangement of these ceramic papers in a metal casing, would prevent the formation of a soot cake during filtration in a DPF unit and, consequently, would avoid a pressure drop in the engine exhaust pipe. Table 3 lists the main features of the ceramic papers. As observed by the SEM image (Figure 6e), X-ray tomography revealed a high porosity of the ceramic paper structure: 75% (Figure 6f and Table 3). Additionally, mechanical properties (elastic modulus and tensile index) indicated a flexible structure, consistent with photos shown in Figure 6c,d.

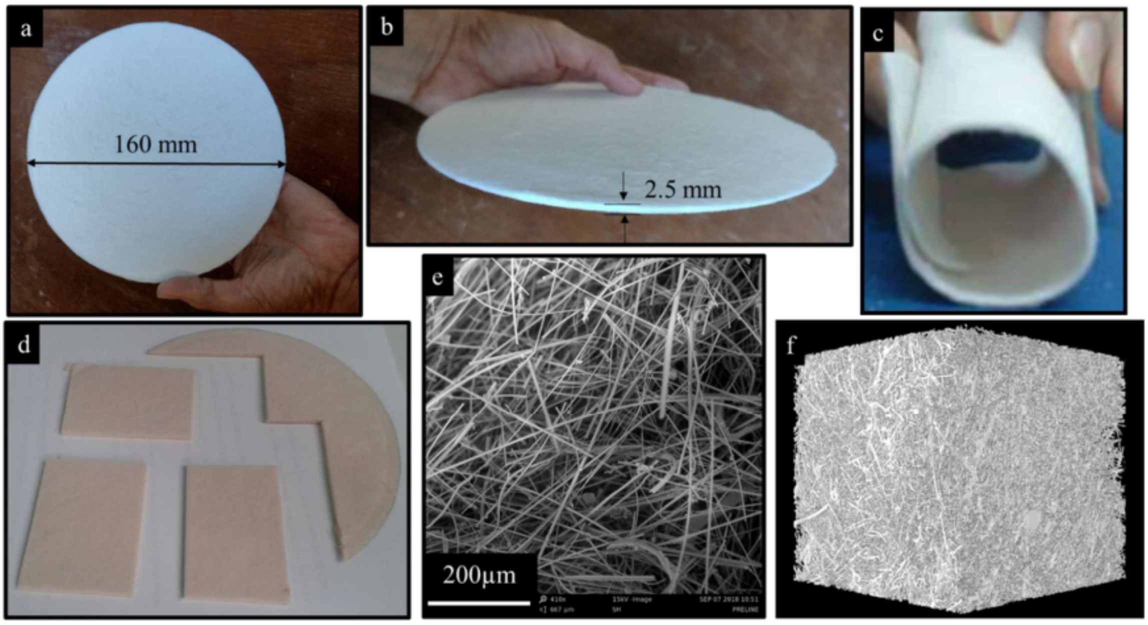

Figure 6. Ceramic paper discs after calcination at 600 °C. (**a**–**d**) Photographs, (**e**) SEM image and (**f**) X-ray tomography.

Table 3. Ceramic-papers properties.

Feature	Value	References
Thickness	2.5 mm	-
Grammage	550 $g \cdot m^{-2}$	-
Porosity *	75%	[44]
Pore size (Average)	25.8 µm	[44]
Permeability (Payri equation parameters) **	$a = 2 \times 10^{-10}$ $b = 0.0013$	[37]
Density	0.22 $g \cdot cm^{-3}$	-
Particle trapping capacity (measured by opacity)	0.6 m^{-1}	[16]
Elastic module ***	0.76 MPa	[45]
Tensile index ***	0.05 $N \cdot m \cdot g^{-1}$	[45]

* Calculated from X-ray tomography; ** $\Delta PDPF = a \cdot Q + b \cdot Q2$; *** Calculated from data obtained from tests on the INSTRON 3344 universal testing machine, using a 1000 N load cell, according to the TAPPI T 576 pm-07 standard method.

An important issue to be taken into account is the thermal stability, because, although the normal temperature of the exhaust gases is between 300 and 400 °C (depending on the type of diesel engine), it can reach higher values (hot spots). In this sense, in a previous work [15], this issue was tested with very promising results.

The morphological and physicochemical characteristics of catalytic ceramic papers play a crucial role in terms of particulate-matter filtering capacity and catalytic burning activity. These properties are very important in a catalytic filter (CDPF) because they determine the filtration efficiency and the possibility of in-situ regeneration of the filter.

2.2.2. Filtration Efficiency of Catalytic Paper

Figure 4 indicates that BenchSoot particles are between 8 and 57 nm (with an average size of 24 nm) and pore sizes of ceramic papers are about 25.8 µm average. Thus, we performed preliminary experiments at bench scale, in which we measured the capacity of filtration using an opacimeter, as described in Materials and Methods. Table 3 shows the particle trapping capacity, where it can be seen that our DPF prototype is capable of filtering small particles at a level below the standards of EURO V (0.6 cm^{-1}). This demonstrates that, despite having a high porosity, ceramic papers have a tortuous structure that can effectively act as a deep bed filter. It should be mentioned that the size of the soot particulates emitted from the test engine we used are in the range of those emitted from most of the modern diesel engines. In a recent article, Wihersaari et al. [46] reported that, at acceleration and constant speeds, particle emissions were composed of non-volatile soot particles, mostly bigger than 50 nm. In contrast, during engine operation, the particle size distribution was bimodal, with a maximum at 10–20 nm and another at 100 nm. In the same vein, Rossomando et al. [47], in a recent work, reported a detailed study in which they characterized ultrafine particles emitted by a light diesel engine with a typical DPF. They found that he highest efficiencies (close to 99%) were detected in the 20–40 nm range, which is similar to that shown for BenchSoot particles, which highlights the potential applicability of the system here reported.

2.2.3. Catalytic Ceramic Paper

In a previous work of the laboratory group [32], an exhaustive characterization of the catalysts prepared and applied in the present work was carried out, and the characteristics described below were found. It is important to highlight that, for both catalysts Co,Ce-PN and Co,Ba,K-PN, the impregnation technique allowed the deposition of the catalytic components through the entire thickness of the ceramic-paper discs.

Co,Ce-PN

In the sample containing Ce and Co, the presence of CeO_2 fluorite and Co_3O_4 spinel was found by FTIR, XRD and TPR [32]. On the other hand, SEM and EDX (mapping) showed an open array of ceramic fibers (SiO_2-Al_2O_3) joined by CeO_2 aggregates (>10 µm), which mainly accumulated at the fiber junctions. In such a structure, the ceramic fibers were partially uncovered with the catalytic particles, which mainly accumulated on CeO_2 binder aggregates.

Co,Ba,K-PN

In the sample containing Co, Ba and K, the presence of CeO_2 fluorite, Co_3O_4 spinel, $BaCO_3$, $BaCoO_{3-y}$ perovskite-type oxide and KNO_3 was found by FTIR, XRD and TPR analysis. In addition, when studying the distribution of the catalytic particles by EDX (mapping), it was observed that cobalt, barium and potassium were homogeneously distributed along the structure covering both fibers and binder agglomerates, in contrast to that observed for the Co,Ce-PN sample. The better covering in the K-containing catalyst is very likely linked to the existence of low-melting-point potassium compounds, enhancing the spreading of catalytic compounds all along the structure. From Co,Ce-PN and Co,Ba,K-PN XRD diffractograms, crystallite sizes of CeO_2 of 7.90 nm and 7.00 nm, respectively, were calculated.

2.3. Catalytic Combustion of the Different Types of Soot Impregnated on Different Structured Systems

2.3.1. Bare Ceramic Papers without Binder

Since the binder (CeO_2 nanoparticles) may contribute to catalytic activity, blank tests were carried out by means of TPO using bare ceramic papers (containing neither catalyst nor binder, i.e., "P" samples). Figure 7 shows TPO profiles and Table 4 summarizes the T_M values obtained for soot combustion over ceramic papers without binder. During the

TPO experiments, the oxidation of soot occurs along with the combustion of hydrocarbon compounds on the surface of soot particles, either with the soot collected during the bench scale assays or after the incorporation of the PM in laboratory conditions (LabSoot and Printex U). Accordingly, the TPO profiles comprise all these contributions and can be deconvoluted into several peaks, where the higher temperature ones correspond to the combustion of the carbonaceous part of the soot particles while the other lower temperature ones can be attributed to unburned hydrocarbons adsorbed or condensed on the soot.

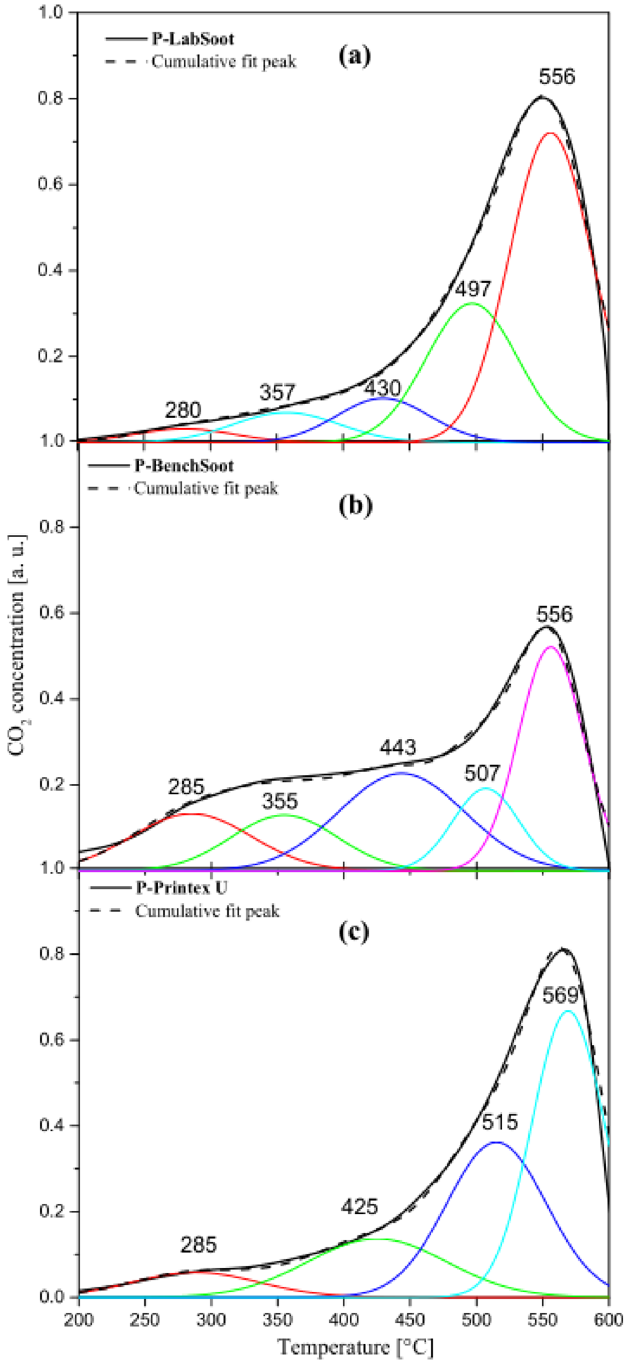

Figure 7. Catalytic activity of ceramic papers without binder (blank tests): (**a**) P-LabSoot, (**b**) P-BenchSoot and (**c**) P-Printex U. Feed composition: 0.1% NO + 18% O_2 balanced in He. The maxima of each deconvolution peak are indicated and the description is shown in Table 4.

Table 4. Maximum combustion rate temperatures of the different fractions of soot deposited on ceramic papers without binder (from deconvoluted curves of Figure 7).

Component Combustion	**Soot Samples**		
	P-LabSoot, T_M [°C]	**P-BenchSoot, T_M [°C]**	**P-Printex U, T_M [°C]**
Adsorbed HC	280 *	285	285 *
Condensed HC	357	355	Not detected
Amorphous carbon	430	443	425
Graphitic carbon tight contact **	497	507	515
Graphitic carbon loose contact **	556	556	569

* This peak corresponds to residual amounts of the solvent used to incorporate soot to ceramic papers [48]. ** Graphitic carbon in tight or loose contact to bare ceramic paper (bare matrix of SiO_2-Al_2O_3 fibers).

From deconvoluted profiles, a peak at about 560 °C, associated to the combustion of the graphitic fraction of carbon (G peak of Figure 3 and Table 1) [49] and another contribution about 497–515 °C, are observed. These peaks could be associated to the burning of the graphitic fraction of soot under loose and tight contact with the bare ceramic paper, respectively, since a small catalytic contribution of the bare support is expected. The different temperatures of the maximum combustion rate of the graphitic portion of the soot in close contact with the paper for the three soot samples (maxima at 497, 507 and 515 °C for LabSoot, BenchSoot and Printex U, respectively) show a correlation in reactivity with the FTIR results. This corroborates that the presence of surface oxygenated compounds favors soot combustion, according to Song et al. [38], who found that elevated soot reactivity is related to oxygenated species in primary soot particles. This agrees with SDTA experiments (Figure 1b), where maxima between 525 and 540 °C were observed in the corresponding profiles, which approaches the combustion of the graphitic part of soot.

In addition, another contribution at intermediate temperatures should be considered in the deconvolution of TPO profiles (Figure 7), due to the presence of amorphous carbon (D3 peak of Figure 3 and Table 1) [49]. Thus, the peaks observed at 430, 443 and 425 °C for LabSoot, BenchSoot and Printex U, respectively (Figure 7), may be related to the burning of the amorphous carbon fraction. It should be noted that the area of this peak for the LabSoot sample is significantly lower than that of BenchSoot or Printex U, which is consistent with results obtained by LRS that showed much less amorphous and disordered carbon percentages for LabSoot (%AC and I_{D1}/I_G, Table 2). In addition, as observed by TEM (Figure 5), the graphitization order was LabSoot > Printex U > BenchSoot, which agrees with the order of T_M for graphitic to amorphous carbon observed for LabSoot, Printex U and BenchSoot when comparing the areas of graphitic and amorphous peaks in the deconvoluted curves of Figure 7.

Additionally, the signals between 400 and 600 °C in the TPO profiles (Figure 7) could involve CO_2 generation due to different processes [50–53]. As reported, the oxidation mechanisms proceed through redox cycles in the 300–500 °C range, where lattice oxygen is the “active oxygen” for soot oxidation at moderate temperatures. At higher temperature, gas-phase radicals play a key role. According to this, both the peaks between 425 and 443 °C and those between 497 and 515 °C would correspond to the CO_2 produced via redox mechanisms, with the peaks between 556 and 569 °C to CO_2 originated by gas-phase free radicals.

On the other hand, as observed by XRF, both BenchSoot and LabSoot showed similar ash compositions, despite the presence of Mn in the former. Nevertheless, they did not influence soot reactivity, as Figure 7 and Table 4 show, probably due to their low content.

In addition, in the TPO profiles of both BenchSoot and LabSoot (Figure 7), broad peaks centered at 355 °C can be considered, being more intense for BenchSoot. These peaks can be assigned to the combustion of hydrocarbons condensed around the carbonaceous core, in consistency with SDTA profile of BenchSoot, which shows peaks at 330 and 380 °C

(Figure 1b) and FTIR spectra for LabSoot and BenchSoot (Figure 2). However, this peak at 355 °C was not observed in the TPO profile of Printex U due to the absence of condensed hydrocarbons in this artificial sample (Figure 1), which could be the reason for the higher temperature for the combustion of the graphitic fraction under loose contact observed for Printex U (Figure 7, peak at 569 °C). Thus, the combustion of these hydrocarbons could help to increase the local temperature, favoring the combustion of graphitic carbon.

On the other hand, it should be noted that a small production of CO_2 at ca. 280 °C should be considered in the TPO profiles of LabSoot and Printex U, which could be ascribed to the residual amounts of n-hexane used to incorporate soot particles to ceramic-paper discs. For the BenchSoot collected from the exhausts at low temperatures, the peak at 285 °C should be attributed to adsorbed hydrocarbon compounds found in large amounts and originated by the incomplete combustion of the fuel and oil residuals [31].

2.3.2. Bare Ceramic Papers with Binder and Catalytic Ceramic Papers

Figure 8 shows the TPO profiles of the different soot samples loaded on ceramic papers only containing ceria nanoparticles as binder. In comparison to the combustion of diesel soot incorporated into ceramic papers without the binder (Figure 7), an improvement in diesel-soot combustion is observed when ceria nanoparticles are added (Table 5 and Figure 8) for all samples, since all the contributions shifted to lower temperatures. Comparing Figures 7 and 8, the peak attributed to graphitic carbon in loose contact with the support shifts to around 75 °C when ceria is added as binder. This behavior is attributed to both CeO_2 oxygen-storage capability and the Ce^{3+}/Ce^{4+} redox couple [15]. An interesting feature is the even greater enhancement observed in soot combustion for the BenchSoot sample, probably related to the presence of the oxygenated compounds detected by FTIR and to the combustion of the condensed hydrocarbons, favored by the presence of CeO_2.

Table 5. Soot deposited on ceramic papers with CeO_2 binder: Maximum combustion rate temperatures (T_M) of the different fractions soot *.

Component Combustion	**Soot Samples**		
	PN-LabSoot, T_M [°C]	**PN-BenchSoot, T_M [°C]**	**PN-Printex U,T_M [°C]**
Adsorbed HC	255	259	253
Condensed HC	302	304	Not detected
Amorphous carbon	392	368	387
Graphitic carbon tight contact	447	426	443
Graphitic carbon loose contact	491	476	492

* TM values obtained from deconvolution curves (Figure 8).

The TPO profiles of soot combustion over catalytic ceramic papers depicted in Figure 9 and Table 6 summarize soot T_M values obtained from Figures 8 and 9 for the combustion of the graphitic fraction of soot. For BenchSoot and LabSoot, a decrease in T_M is observed only when Co, Ba, K is added. However, only small differences between the maximum combustion rate temperatures for Co,Ce-PN samples are observed as compared to PN samples. This behavior can be related with the distribution of the catalyst over the ceramic structure. As discussed in Section 2.2.3, samples containing K help to improve the distribution of the active phases and improving soot-to-catalyst contact during TPO evaluations. This is especially important for LabSoot, since the mobility of the K salts favors the combustion of graphitic carbon, which is present in a higher proportion in this type of soot compared to BenchSoot or Printex U. In addition, the presence of the $BaCoO_{3-y}$ perovskite detected by TPR could contribute to the high catalytic activity and stability obtained for Co,Ba,K-PN, since this mixed oxide helps to trap and release NO_X and, thus, benefit soot combustion [32,54].

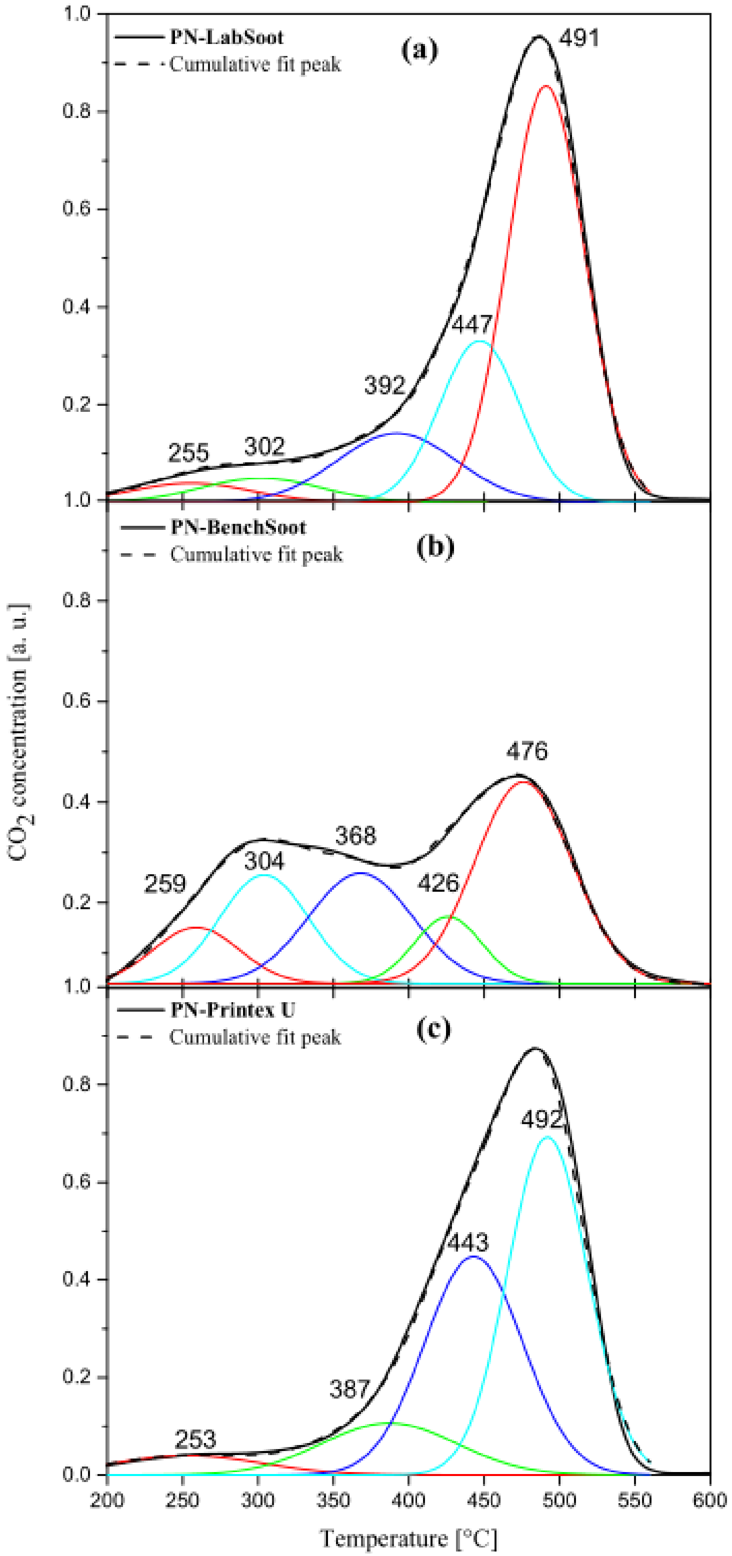

Figure 8. Deconvolution of TPO profiles for diesel-soot combustion: Catalytic activity of ceramic papers with binder: (**a**) PN-LabSoot, (**b**) PN-BenchSoot, and (**c**) PN-Printex U samples. Reactor inlet composition: 0.1% NO + 18% O_2 balance in He. The maxima of each deconvolution peak are indicated and the description is shown in Table 5.

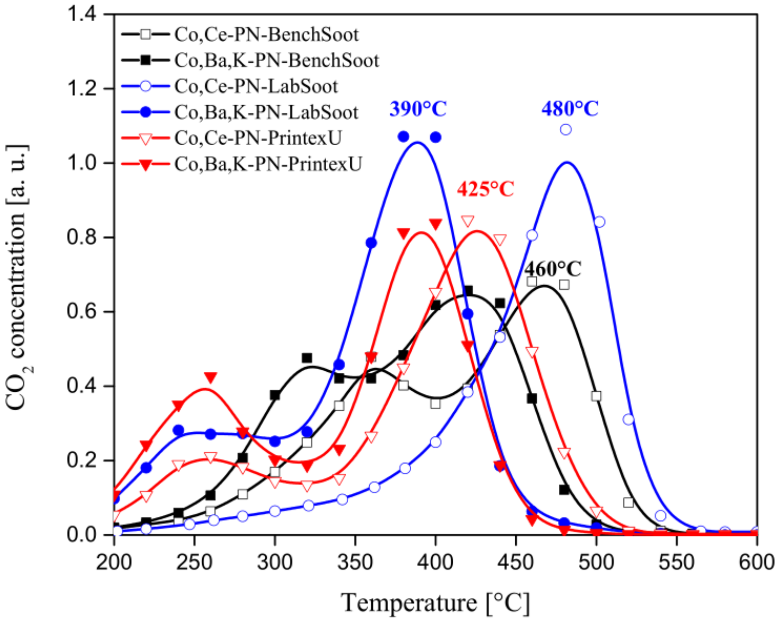

Figure 9. Activity of catalytic ceramic papers (Co,Ce and Co,Ba,K) for the combustion of different types of soot particles. Reactor inlet composition: 0.1% NO + 18% O_2 balance in He.

Table 6. Catalytic combustion of soot: comparison of the activity of ceramic papers (PN) and catalytic ceramic papers.

Catalyst	Maximum Combustion Rate Temperature [°C] (T_M) *		
	LabSoot	BenchSoot	Printex U
PN	491	476	492
Co,Ce-PN	480	472	425
Co,Ba,K-PN	390	427	390

* T_M values obtained from deconvolution curves (Figures 8 and 9). Only temperatures of maximum combustion rate of the graphitic fractions of soot are compared.

On the other hand, for Printex U combustion, an improvement in the catalytic behavior is observed with the addition of either Co,Ba,K or Co,Ce catalysts, with Co,Ba,K-PN being more active than the Co,Ce catalyst (Co,Ce-PN). As this model type of soot does not contain either surface oxygenated compounds or adsorbed HC, both catalysts (Co,Ba,K-PN and Co,Ce-PN) help soot burning by supplying oxygen.

Considering the primary particle sizes of soot, LabSoot exhibits the largest particles, for which the catalyst containing potassium enhances soot-to-catalyst contact and favors soot combustion. On the other hand, BenchSoot exhibits the smallest particles and graphene layers are not so ordered as for LabSoot, for which BenchSoot shows the lowest T_M value for PN.

The soot-to-catalyst contact plays a key role in catalyst performance. Tight contact improves the reaction rate compared to loose contact, whereas the real contact type of a catalyst and particles in a DPF device is similar to loose contact [55]. However, the high exhaust gas temperatures would allow the soot to burn when collected, thus preventing the formation of a cake.

To evaluate the influence of the contact between soot and catalysts on catalytic performance, both Co,Ce and Co,Ba,K systems with soot collected from bench tests were milled in an agate mortar to improve soot–catalyst contact and then evaluated by TPO assays. These samples were distinguished by adding "-M" and the corresponding TPO profiles and T_M values are shown in Figure 10 and Table 7.

Table 7. Temperatures of maximum soot combustion rates on catalytic ceramic papers with BenchSoot (obtained from Figure 10). Effect of soot-to-catalyst contact.

Combustion Component	**Co,Ba,K-PN-BenchSoot *** **T_M [°C]**	**Co,Ba,K-PN-BenchSoot-M **** **T_M [°C]**
Adsorbed HC	253	254
Condensed HC	320	316
Amorphous carbon and Graphitic carbon tight contact	377	396
Graphitic carbon loose contact	427	
	Co,Ce-PN-BenchSoot *	Co,Ce-PN-BenchSoot-M **
Adsorbed HC	270	267
Condensed HC	328	328
Amorphous carbon	367	364
Graphitic carbon tight contact	428	411
Graphitic carbon loose contact	472	453

* As collected from the test bench. ** Collected from the test bench and milled prior to TPO runs.

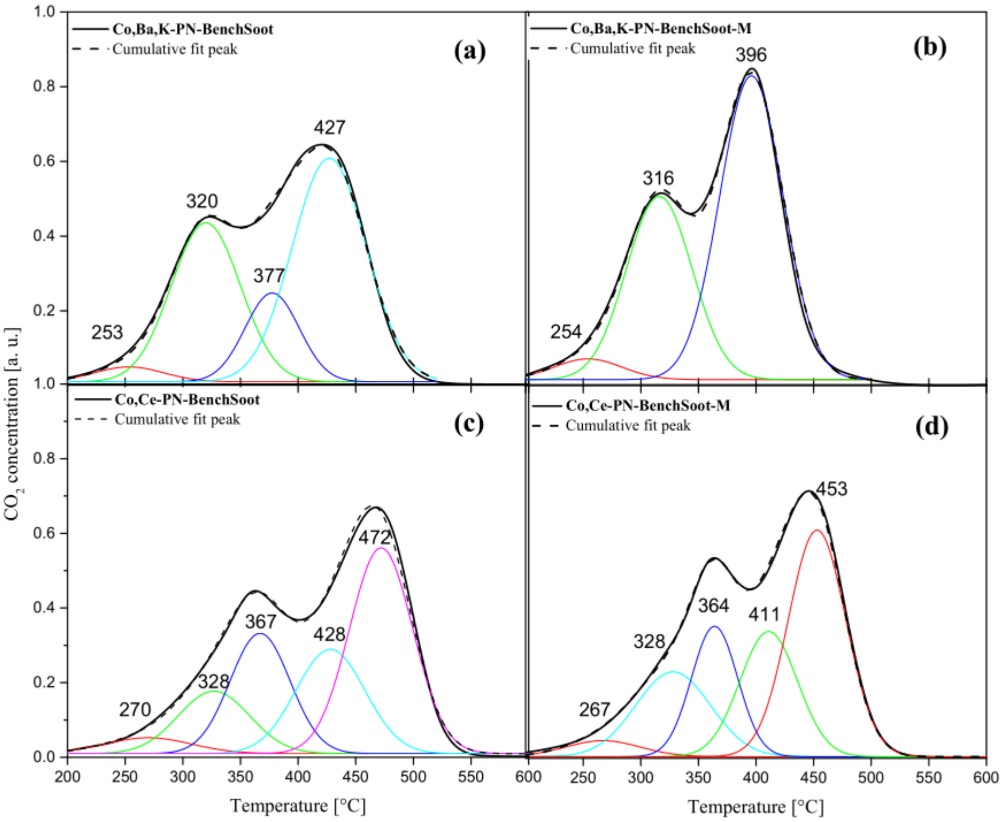

Figure 10. Soot-to-catalyst contact effect. Deconvolution of TPO profiles for BenchSoot combustion over catalytic ceramic papers with Co,Ba,K or Co,Ce: (**a**,**c**) loose contact, (**b**,**d**) tight contact (milled samples). Reactor inlet composition: 0.1% NO + 18% O_2 (He balance). The maxima of each deconvolution peak are indicated and the description is shown in Table 8.

The TPO profile observed for the Co,Ba,K catalyst (Figure 10a) was deconvoluted considering four contributions, with maxima at 253, 320, 377 and 427 °C. If compared with the deconvolutions displayed in Figure 8 and Table 5, the presence of Co, Ba, K originates the process during which both amorphous and graphitic carbon in close contact with the catalyst oxidizes at the same temperature. In tight-contact conditions (Figure 10b), the combustion of all fractions of soot (graphitic and amorphous carbon) burn together at the same temperature (T_M = 396 °C), for which the TPO could be deconvoluted only considering three contributions with maxima at 254, 316 and 396 °C. In the case of the Co,Ce catalyst, an enhancement of catalytic activity was also observed for the soot-impregnated and ground catalyst, as the peaks associated with the graphitic carbon fraction in looser and tighter contact with the catalyst (T_M = 472 and 428 °C) shift to lower temperatures (T_M = 453 and 411 °C) as contact conditions improve. In contrast to the observed for Co,Ba,K catalyst, these high-temperature peaks do not merge into one peak.

Taking into account that the oxidation of soot involves contact among three phases (two solids and gaseous oxygen), the milling process enhances the soot-to-catalyst contact and decreases T_M values. However, as Figure 10 shows, the shift to lower temperatures for milled samples is observed only in the high-temperature peaks (ascribed to the combustion of the graphitic fraction of soot). The low-temperature peaks (associated to the burning of the amorphous fraction of soot and condensed and adsorbed hydrocarbons) do not shift after milling the structured catalyst-soot samples.

Table 8 shows a comparison between the maximum combustion rate temperatures obtained with the catalysts reported in this work and others taken from the literature. Although T_M depends on the reaction conditions such as the amount of catalyst, metal loadings, gaseous flows and type of soot, it can be observed that the values obtained with our catalysts are in good agreement with those reported by other authors [9,12,56–60].

Table 8. Catalytic activity compared with selected catalysts reported for soot combustion.

Catalyst/Support	T_M (°C)	Oxidizing Flow	References
Co,Ba,K/CeO_2	370	4% NO + 18% O_2	[56]
Co,Ba,K/α-Al_2O_3	450	Air	[57]
Co,Ba,K/ZrO_2/Metallic foam	380	0.1% NO + 18% O_2	[12]
Co,Ba,K/ceramic paper with CeO_2	390	0.1% NO + 18% O_2	This article
Co,Ba,K/ZrO_2/Cordierite monolith	400	0.1% NO + 18% O_2	[9]
Co,Ce/ceramic paper with CeO_2	480	0.1% NO + 18% O_2	This article
Co,Ce/Ni nanosheet	430	600 ppm NO + 10% O_2	[58]
K/MnO_2	490	10% O_2	[59]
Pt/$LaCoO_3$	393	Air	[60]

3. Materials and Methods

3.1. Diesel Soot Acquisition

Carbonaceous particles originated in the combustion of diesel fuel were collected in two ways: from diesel fuel burned inside a beaker at lab level (LabSoot), and from the exhausts of a bench diesel engine (BenchSoot). These two samples were compared with a carbon black model (Printex® U) provided by Evonik Degussa (Essen, Germany), which, according to the literature, represents diesel soot [43,61,62].

The artificial soot (LabSoot) was prepared by burning commercial diesel fuel (YPF, Argentina, sulfur content: 6 ppm) in a glass beaker. After fuel burning, the soot formed was collected from the vessel walls and dried in an oven during 24 h at 120 °C.

On the other hand, from the working engine fueled with the same diesel fuel used to obtain LabSoot, real soot (BenchSoot) was collected as follows. A cartridge in which eight square (11 cm side) catalytic ceramic-paper pieces were placed conforming a filter, as depicted in Figure 11, was connected to a Fiat 1.7 Td engine mounted on a test bench (Figure 12). Soot sampling and opacity measurements were simultaneously performed. The assay was conducted following the snap-acceleration smoke procedure, according to J1667 SAE norms, during which the maximum temperature the external cartridge wall reached was 280 °C with the engine working at 3800 rpm. Opacity measurements performed and reported elsewhere [16] showed a satisfactory filtration capacity of catalytic ceramic papers, as opacity values close to those established by EURO V standards for vehicles were achieved. After the assay, the filter was disassembled and portions of the catalytic papers loaded with soot particles (16 mm diameter circles) were cut for catalytic laboratory experiments (Figure 12c).

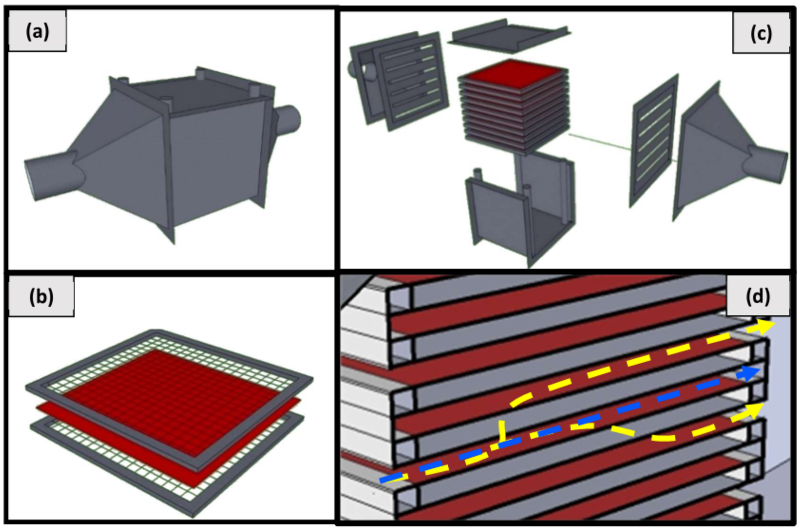

Figure 11. Scheme of the metallic support for soot particle collection in the test bench. (**a**) Metallic cartridge, (**b**) ceramic paper (🟥) between metal meshes (▦), (**c**) exploded view and (**d**) alternately plugged channels and exhaust flowing.

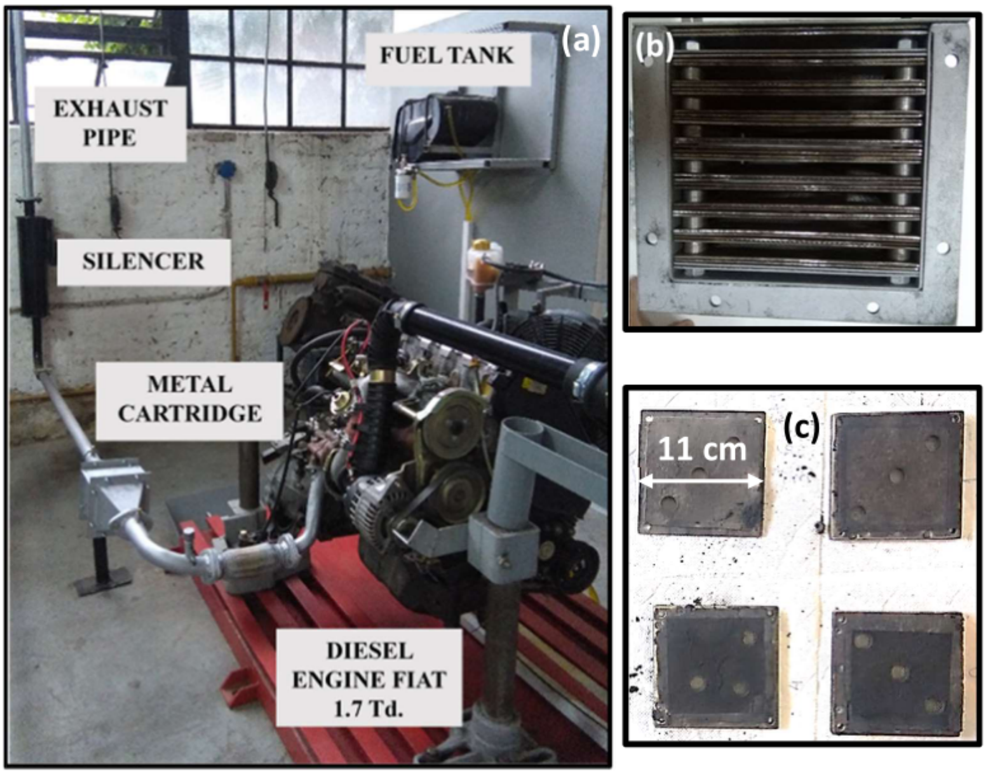

Figure 12. (**a**) Bench engine with metallic cartridge coupled; (**b**) front view of eight ceramic papers between meshes stacked inside the metal cartridge; (**c**) catalytic ceramic papers after test bench assay from which samples of 16 mm were extracted for catalytic laboratory TPO tests.

3.2. Preparation of Catalytic Ceramic Papers

Ceramic papers were prepared according to the papermaking technique first reported by Ichiura et al. [63] and further adapted in previous works [17,32]. The method involves the addition of cationic and anionic polyelectrolytes in order to enhance the retention of components during the papermaking process.

The catalytic ceramic papers were synthesized in three steps. (i) Preparation of ceramic-paper discs, according to the standard norms (SCAN-C 26:76 and SCAN-M 5:76) typical in the manufacture of conventional paper, partially replacing cellulosic fibers by ceramic ones and incorporating polyelectrolytes, (ii) calcination treatment at 600 °C for 2 h and (iii) incorporation of active phases by dripping precursor solutions followed by another calcination treatment. The steps are described in detail in the following items.

3.2.1. Preparation of Ceramic Papers

Ceramic-paper discs were prepared according to a method that consists of dispersing in a dilute NaCl aqueous solution (0.01 M) both cellulosic and ceramic fibers (50 wt.% SiO_2-48 wt.% Al_2O_3), also adding 20 wt.% of CeO_2 nanoparticles (Nyacol) as binder compound, which helps increase the mechanical resistance of ceramic papers, as previously reported [17]. In addition, two polyelectrolytes were added to favor inorganic material retention during the filtration step, one cationic and another anionic: polyvinylamine (PVAm) and polyacrylamide (A-PAM).

Following the papermaking technique, a sheet of 16.5 cm diameter was formed. After drying in a chamber with controlled atmosphere (23 °C, 52% relative humidity, 24 h), they were calcined in air at 600 °C for 2 h. The ceramic papers thus obtained were named PN.

3.2.2. Active Phase Impregnation

Two types of catalysts were prepared from the incorporation of different catalytic elements in to the ceramic papers, one by adding cobalt, barium and potassium and the other by the incorporation of cobalt and cerium, all of them from their corresponding nitrate solutions, by drip impregnation. The impregnated papers were first dried in an oven at 120 °C during 12 h and then calcined at 600 °C for 2 h. It should be noted that, for the second type of catalyst, Ce oxide (Nyacol) was also present in the ceramic paper structure as it had been added as a binder for both formulations.

Mixed solutions of Co and Ce (Co:Ce wt. ratio = 1:2.37) and Co, Ba and K (Co:Ba:K wt. ratio = 1:1.33:0.58) were used, obtaining a loading of 5% wt./wt. of active phases. The ceramic papers thus obtained were named Co,Ce-PN and Co,Ba,K-PN, respectively.

3.2.3. Ceramic Papers without Binder

As blank samples for catalytic evaluations, ceramic papers without CeO_2 Nyacol binder were prepared. The procedure was identical to that described in Section 3.2.1, except for the addition of CeO_2 Nyacol. Calcined papers were called P.

3.3. Characterization Techniques

3.3.1. Soot Characterization

The functional groups of the species adsorbed on the soot particles were identified using FTIR technique. Samples diluted in KBr (approximately 1% sample in KBr) were pressed into wafer form. Infrared spectra were acquired on a Shimadzu Prestige-21 IR spectrometer, Kyoto, Japan. For all spectra 40 scans were accumulated, working with a resolution of 8 cm^{-1}.

LRS was used to study the degree of carbon ordering in different soot samples. Spectra were obtained using Horiba JOBI YVON LabRAM HR equipment, Kyoto, Japan. The 514.5 nm line, generated by a Spectra 9000 Photometrics Ar ion laser, was used as the excitation source, adjusting the laser power to 30 mW. In all cases, several spectra were acquired for each sample.

The elements present in the samples between Na23 and U92 were identified by XRF using a Shimadzu spectrometer (EDX-720, Kyoto, Japan). In addition, weight percentages were approximately calculated. To this aim, a quantification method that uses the theory of X-ray fluorescence emission, without using external standards, was used.

The transformations of diesel soot samples during heating treatments in air were studied by thermogravimetric techniques using a TGA/SDTA 851(Mettler Toledo, Columbus, OH, USA). For this purpose, 3 mg of soot particles (LabSoot or Printex U) or 10 mg of sample (ceramic paper with BenchSoot) were used. The temperature program employed consisted of heating the samples from 25 to 750 °C, with a temperature ramp of 10 $°C·min^{-1}$, in air flow (60 $mL·min^{-1}$).

Using a JEOL JEM-2100 Plus transmission electron microscope (JEOL, Tokyo, Japan), HR-TEM images were obtained. The accelerating voltage was 200 kV. The samples were sonicated in isopropyl alcohol for several minutes. A copper grid (300 mesh) was used on which a drop of the obtained suspension was deposited with a carbon film and allowed to evaporate. GATAN Digital Micrograph software version 2.32.888.0 (GATAN Inc., Pleasanton, CA, USA) was used to size the soot particles. At least 200 randomly selected individual primary particles were measured and the average particle size was calculated.

3.3.2. Soot Reactivity

Artificial soot particles (LabSoot or Printex U) were dispersed in an organic solvent (n-hexane) to obtain a 600 ppm suspension of diesel soot in n-hexane and an ultrasonic bath was used to homogenize it. The incorporation of the soot particles into the ceramic paper pieces (16 mm diameter discs) was carried out by dripping the suspension until saturation. The pieces of ceramic paper were then placed face down and the procedure was repeated. Once impregnated on both sides, the samples were dried at room temperature.

Soot particles obtained from the diesel engine (BenchSoot) were filtered and collected either on ceramic or catalytic ceramic papers, as described in Section 3.1. In the last case, catalytic ceramic papers were set in the case, alternating those containing Co,Ce and those with Co,Ba,K, so as to study both catalytic ceramic papers under the same experimental conditions. Portions of these papers loaded with soot were cut into 16 mm diameter discs (Figure 12c).

The reactivity of these soot types loaded on catalytic papers was studied by TPO. For this purpose, three stacked disks of the soot-loaded structured samples were heated from 25 °C to 600 °C in a flow of O_2 (18%) + NO (0.1%) diluted in He (total flow 20 $mL·min^{-1}$) at a heating rate of 5° $C·min^{-1}$, in a flow-through apparatus. The gases generated were analyzed chromatographically with a Shimadzu GC-2014 apparatus equipped with a thermal conductivity detector (TCD) and using a Porapak Q column.

Soot conversion was determined from the chromatogram obtained at each temperature. For this purpose, the area of the CO_2 peak was measured, with the amounts of CO produced being negligible. The TPO curves showed the CO_2 produced at each temperature and the maximum soot burning rate was determined by the maximum of the TPO peak (T_M).

3.3.3. Ceramic-Paper Characterization

Mechanical properties. The tensile strength and elastic modulus of ceramic paper were determined with an INSTRON 3344 universal tester, equipped with a 1000 N load cell at a speed of 50.8 $mm·min^{-1}$, using the standard TAPPI T 576 pm-07 method, commonly used for tissue paper. Sheets of ceramic paper about 2.5 mm thick were cut into rectangles 50 mm wide and 70 mm long, leaving a free length of 50 mm between the test jaws.

SEM images were acquired with a Phenom World Pro X machine operating at an acceleration of 20 kV and were used to study the morphology of the samples.

Permeability. Bench-scale ceramic paper pressure drop measurements were performed on a Flujo Tech 600 flowmeter (Horacio Resio Devices), which is used for flow analysis in real engines [64]. Permeation curves were obtained by plotting the permeated air flow rate as the air pressure varied.

X-ray Tomography. Micro-computed tomography (micro-CT) was used to obtain 3D X-ray imaging so as to determine porosity and to measure the size of the inter-fiber voids. A Bruker SkyScan 1172 apparatus was used, selecting the source voltage of 44 kV and using a current of 226 µA. An image was recorded every 0.2°, with a spatial resolution of 2.07 µm pxl^{-1} and from these, the 3D structure was reconstructed using Bruker NRecon software.

4. Conclusions

Depending on the origin of the soot particles, their composition differs and, consequently, their oxidation characteristics vary. They basically consist of an amorphous carbon core surrounded by a graphitic carbon layer on which different types of species are adsorbed. Comparing the samples studied, LabSoot has proportionately more graphitic carbon than BenchSoot, which is more difficult to burn than amorphous carbon. On the other hand, BenchSoot presents more quantities of condensed hydrocarbons than LabSoot, mainly aliphatic HC, though LabSoot exhibited larger amounts of oxygenated species. In the case of the Printex U sample, it contains proportionately more graphitic than amorphous carbon, and did not show condensed hydrocarbons, for which we can establish the following graphitization order: LabSoot > Printex U > BenchSoot.

Both Co,Ce and Co,Ba,K structured catalysts exhibited reducibility properties that helped the oxidation of soot via redox mechanisms, which, in addition to the oxygen storage capacity of CeO_2 nanoparticles, allowed the catalytic burning of the different types of soot samples studied. The Co,Ce system preferentially improved T_M for the Printex U sample since it helped supply active oxygen, absent in the surface of this model-type soot. On the other hand, the Co,Ba,K catalyst showed a higher catalytic effect on LabSoot since this type of soot exhibited the largest primary particles and the higher order of graphene layers, for which the catalyst containing potassium enhances soot-to-catalyst contact and favors soot combustion. For Co,Ba,K-ceramic paper, T_M values between 390 and 425 °C were observed for both LabSoot and BenchSoot samples, which are close to the diesel exhaust gas temperature. Considering that the new generations of diesel engines produce lower amounts of NOx, the transfer and reactivity of oxygen adsorbed on the catalyst to the soot particles become increasingly important in order to decrease the regeneration temperature of the filter.

Author Contributions: S.A.L. carried out the experiments and the editing of a draft document. E.E.M. contributed to discussions and the interpretation of results and editing of the final version. V.G.M., project director, contributed to discussions and the interpretation of results and editing of the final version. All authors have read and agreed to the published version of the manuscript.

Funding: The authors thank the financial support received from Agencia Nacional de Promoción Científica y Tecnológica (ANPCyT, grant PICT 2019-00976), Consejo Nacional de Investigaciones Científicas y Técnicas (CONICET) and Universidad Nacional del Litoral (UNL, CAI+D2020).

Data Availability Statement: All data and materials support the published claims and comply with field standards.

Acknowledgments: The authors would like to thank the Grant PME 87-PAE 36985 to purchase the Raman Instrument, to the teachers of Escuela Industrial Superior (EIS, FIQ-UNL) for the collaboration in the experiments at bench scale and also to the Institute of Cellulose Technology (ITC, FIQ, UNL), for the infrastructural facilities for the preparation of ceramic papers.

Conflicts of Interest: The authors declare no conflict of interest.

References

1. Zhang, Y.; Zhang, R.; Rao, L.; Kook, S. *A Comparison between In-Flame and Exhaust Soot Nanostructures in a Light-Duty Diesel Engine*; SAE Technical Paper; SAE International: Warrendale, PA, USA, 28 March 2017. [CrossRef]
2. Lee, S.; Lim, S.; Lee, H.; Park, S. Probing the oxidation reactivity of ultra-low-sulfur diesel soot with controlled particle size and organic mass fraction. *J Anal. Appl. Pyrolysis* **2019**, *140*, 264–273. [CrossRef]
3. Neeft, J.P.A.; Makkee, M.; Moulijn, J.A. Diesel particulate emission control. *Fuel Process. Technol.* **1996**, *47*, 1–69. [CrossRef]
4. Stanmore, B.R.; Tschamber, V.; Brilhac, J.F. Oxidation of carbon by NOx, with particular reference to NO_2 and N_2O. *Fuel* **2008**, *87*, 131–146. [CrossRef]
5. Twigg, M.V. Progress and future challenges in controlling automotive exhaust gas emissions. *Appl. Catal. B Environ.* **2007**, *70*, 2–15. [CrossRef]
6. Azambre, B.; Collura, S.; Trichard, J.M.; Weber, J.V. Nature and thermal stability of adsorbed intermediates formed during the reaction of diesel soot with nitrogen dioxide. *Appl. Surf. Sci.* **2006**, *253*, 2296–2303. [CrossRef]
7. Meloni, E.; Palma, V. Most recent advances in Diesel engine catalytic soot abatement: Structured catalysts and alternative approaches. *Catalysts* **2020**, *10*, 745. [CrossRef]
8. Van Setten, B.A.A.L.; Makkee, M.; Moulijn, J.A. Science and technology of catalytic diesel particulate filters. *Catal. Rev. Sci. Eng.* **2001**, *43*, 489–564. [CrossRef]
9. Banús, E.D.; Milt, V.G.; Miró, E.E.; Ulla, M.A. Catalytic coating synthesized onto cordierite monolith walls. Its application to diesel soot combustion. *Appl. Catal. B* **2013**, *132–133*, 479–486. [CrossRef]
10. Palma, V.; Ciambelli, P.; Meloni, E. Influence of operative parameters on microwave regeneration of catalytic soot WFF for Diesel engines. *Chem. Eng. Trans.* **2011**, *25*, 1001–1006. [CrossRef]
11. Banús, E.D.; Sanz, O.; Milt, V.G.; Miró, E.E.; Montes, M. Development of a stacked wire-mesh structure for diesel soot combustion. *Chem. Eng. J.* **2014**, *246*, 353–365. [CrossRef]
12. Banús, E.D.; Milt, V.G.; Miró, E.E.; Ulla, M.A. Co,Ba,K/ZrO_2 coated onto metallic foam (AISI 314) as a structured catalyst for soot combustion: Coating preparation and characterization. *Appl. Catal. A* **2010**, *379*, 95–104. [CrossRef]
13. Koga, H.; Ishihara, H.; Kitaoka, T.; Tomoda, A.; Suzuki, R.; Wariishi, H. NOx reduction over paper-structured fibre composites impregnated with Pt/Al_2O_3 catalyst for exhaust gas purification. *J. Mater. Sci.* **2010**, *45*, 4151–4157. [CrossRef]
14. Cecchini, J.P.; Banús, E.D.; Leonardi, S.A.; Zanuttini, M.A.; Ulla, M.A.; Milt, V.G. Flexible-structured systems made of ceramic fibers containing Pt-NaY zeolite used as CO oxidation catalysts. *J. Mater. Sci.* **2014**, *50*, 755–768. [CrossRef]
15. Tuler, F.E.; Banús, E.D.; Zanuttini, M.A.; Miró, E.E.; Milt, V.G. Ceramic papers as flexible structures for the development of novel diesel soot combustion catalysts. *Chem. Eng. J.* **2014**, *246*, 287–298. [CrossRef]
16. Sacco, N.A.; Banús, E.D.; Milt, V.G.; Miró, E.E.; Bortolozzi, J.P. Catalytic Paper Filters for Diesel Soot Abatement: Studies at Laboratory and Bench Scales. *Emiss. Control. Sci. Technol.* **2020**, *6*, 450–461. [CrossRef]
17. Tuler, F.E.; Gaigneaux, E.M.; Miró, E.E.; Milt, V.G.; Debecker, D.P. Catalytic ceramic papers for diesel soot oxidation: A spray method for enhanced performance. *Catal. Commun.* **2015**, *72*, 116–120. [CrossRef]
18. Leonardi, S.A.; Zanuttini, M.A.; Miró, E.E.; Milt, V.G. Catalytic paper made from ceramic fibres and natural ulexite. Application to diesel particulate removal. *Chem. Eng. J.* **2017**, *317*, 394–403. [CrossRef]
19. Sharma, V.; Uy, D.; Gangopadhyay, A.; O'Neill Paxton, W.; Sammut, A.; Ford, M.; Aswath, P. Structure and chemistry of crankcase and exhaust soot extracted from diesel engines. *Carbon* **2016**, *103*, 327–338. [CrossRef]
20. Bagi, S.; Sharma, V.; Patel, M.; Aswath, P. Effects of diesel soot composition and accumulated vehicle mileage on soot oxidation characteristics. *Energy Fuels* **2016**, *30*, 8479–8490. [CrossRef]
21. He, J.; Li, L.; Feng, H.; Jiang, M.; Li, J.; Guo, L.; Zhang, J.; Zhang, P.; Gong, J.; Huang, Q. Morphology and nanostructure of flame-formed soot particles from combustion of typical municipal solid waste. *Fuel Process. Technol.* **2022**, *232*, 107269. [CrossRef]
22. Kamp, C.J.; Bagi, S.; Wang, Y. *Phenomenological Investigations of Mid-Channel Ash Deposit Formation and Characteristics in Diesel Particulate Filters*; SAE Technical Paper No. 2019-01-0973; SAE International: Warrendale, PA, USA, 2 April 2019. [CrossRef]
23. Hu, Z.; Fu, J.; Gao, X.; Lin, P.; Zhang, Y.; Tan, P.; Lou, D. Waste cooking oil biodiesel and petroleum diesel soot from diesel bus: A comparison of morphology, nanostructure, functional group composition and oxidation reactivity. *Fuel* **2022**, *321*, 124019. [CrossRef]
24. Medalia, A.I.; Rivin, D.; Sanders, D.R. A comparison of carbon black with soot. *Sci. Total Environ.* **1983**, *31*, 1–22. [CrossRef]
25. Meng, Z.; Yang, D.; Yan, Y.; Han, W. Comparison of oxidation characteristics analysis between diesel soot and carbon black. *J. Comput. Sci. Technol.* **2016**, *22*, 71–76. [CrossRef]
26. Bueno-López, A. Diesel soot combustion ceria catalysts. *Appl. Catal. B* **2014**, *146*, 1–11. [CrossRef]
27. Moreno-Román, E.J.; Cruz-López, A.; García-Gómez, C.; Zanella, R.; Suárez-Vázquez, S.I. Evaluation of the catalytic oxidation of soot by CeO_X-$LaMnO_3$ at different O_2 pressures synthesized by ultrasonic-assisted hydrothermal method. *Environ. Sci. Pollut. Res.* **2020**, *7*, 15475–15487. [CrossRef] [PubMed]
28. Zhang, Y.; Zhang, P.; Xiong, J.; Wei, Y.; Jiang, N.; Li, Y.; Chi, H.; Zhao, Z.; Liu, J.; Jiao, J. Synergistic effect of binary Co and Ni cations in hydrotalcite-derived $Co_{2-x}Ni_xAlO$ catalysts for promoting soot combustion. *Fuel* **2022**, *320*, 123888. [CrossRef]
29. Lisi, L.; Landi, G.; Di Sarli, V. The Issue of Soot-Catalyst Contact in Regeneration of Catalytic Diesel Particulate Filters: A Critical Review. *Catalysts* **2020**, *10*, 1307. [CrossRef]

30. Stegmayer, M.A.; Milt, V.G.; Navascues, N.; Gamez, E.; Irusta, S.; Miró, E.E. Cobalt deposited on micro and nanometric structures of ceria and zirconia applied in diesel soot combustion. *Mol. Catal.* **2020**, *418*, 100636. [CrossRef]
31. Liang, X.; Lv, X.; Wang, Y.; He, L.; Wang, Y.; Fu, K.; Liu, Q.; Wang, K. Experimental investigation of diesel soot oxidation reactivity along the exhaust after-treatment system components. *Fuel* **2021**, *302*, 121047. [CrossRef]
32. Leonardi, S.A.; Tuler, F.E.; Gaigneaux, E.; Debecker, D.P.; Miró, E.E.; Milt, V.G. Novel ceramic paper structures for diesel exhaust purification. *Environ. Sci. Pollut. Res.* **2018**, *25*, 35276–35286. [CrossRef] [PubMed]
33. Uy, D.; Ford, M.A.; Jayne, D.T.; O'Neill, A.E.; Haack, L.P.; Hangas, J.; Jagner, M.J.; Sammut, A.; Gangopadhyay, A.K. Characterization of gasoline soot and comparison to diesel soot: Morphology, chemistry, and wear. *Tribol. Int.* **2014**, *80*, 198–209. [CrossRef]
34. Bharti, S.; Kumar, D.; Anand, S.; Barman, S.; Kumar, N. Characterization and morphological analysis of individual aerosol of PM 10 in urban area of Lucknow, India. *Micron* **2017**, *103*, 90–98. [CrossRef] [PubMed]
35. Larkin, P. Infrared and Raman Spectroscopy. In *Principles and Spectral Interpretation*; Elsevier: Amsterdam, The Netherlands, 2011; ISBN 978-0-12-386984-5.
36. Luo, J.; Zhang, Y.; Wang, J.; Zhang, Q. Effect of acetone-butanol-ethanol addition to diesel on the soot reactivity. *Fuel* **2018**, *226*, 555–563. [CrossRef]
37. Toth, A.; Hoffer, A.; Pósfai, M.; Ajtai, T.; Kónya, Z.; Blazsó, M.; Czégény, Z.; Kiss, G.; Bozóki, Z.; Gelensér, A. Chemical characterization of laboratory-generated tar ball particles. *Atmos. Chem. Phys.* **2018**, *18*, 10407–10418. [CrossRef]
38. Song, J.; Alam, M.; Boehman, A.; Kim, U. Examination of the Oxidation Behavior of Biodiesel Soot. *Combust. Flame* **2006**, *146*, 589–604. [CrossRef]
39. Ishiguro, T.; Suzuki, N.; Fujitani, Y.; Morimoto, H. Microstructural changes of diesel soot during oxidation. *Combust. Flame* **1991**, *85*, 1. [CrossRef]
40. Jawhari, T.; Roid, A.; Casado, J. Raman spectroscopic characterization of some commercial, carbon black materials. *Carbon* **1995**, *11*, 1561–1565. [CrossRef]
41. Reich, S.; Thomsen, C. Raman spectroscopy of graphite Phil. *Trans. R. Soc. Lond. A* **2004**, *362*, 2271–2288. [CrossRef] [PubMed]
42. Sadezky, A.; Muckenhuber, H.; Grothe, H.; Niessner, R.; Pöschl, U. Raman microspectroscopy of soot and related carbonaceous materials: Spectral analysis and structural information. *Carbon* **2005**, *43*, 1731–1742. [CrossRef]
43. Arnal, C.; Bravo, Y.; Larrosa, C.; Gargiulo, V. *Correlation between Real Diesel Fouled-EGRc Soot Samples and Soot Surrogates: Reactivity with NO and* O_2 *and Chemical-Physical Characterization*; SAE International: Warrendale, PA, USA, 3 April 2018. [CrossRef]
44. Sánchez, A.; Milt, V.G.; Miró, E.E.; Güttel, R. Ceramic fiber-based structures as catalyst supports: A study on mass and heat transport behavior applied to CO_2 methanation. *Ind. Eng. Chem. Res.* **2020**, *59*, 16539–16552. [CrossRef]
45. Leonardi, S.A. Desarrollo de Papeles Cerámicos Catalíticos Aplicados a Catálisis Ambiental. Ph.D. Thesis, Universidad Nacional del Litoral, Santa Fe, Argentine, 2019. Available online: https://hdl.handle.net/11185/6245.
46. Wihersaari, H.; Pirjola, L.; Karjalainen, P.; Saukko, E.; Kuuluvainen, H.; Kulmala, K.; Keskinen, J.; Rönkkö, T. Particulate emissions of a modern diesel passenger car under laboratory and real-world transient driving conditions. *Environ. Pollut.* **2020**, *265*, 114948. [CrossRef] [PubMed]
47. Rossomando, B.; Meloni, E.; De Falco, G.; Sirignano, M.; Arsie, I.; Palma, V. Experimental characterization of ultrafine particle emissions from a light-duty diesel engine equipped with a standard DPF. *Proc. Combust. Inst.* **2021**, *38*, 5695–5702. [CrossRef]
48. Godoy, M.L.; Banús, E.D.; Sanz, O.; Montes, M.; Miró, E.E.; Milt, V.G. Stacked Wire Mesh Monoliths for the Simultaneous Abatement of VOCs and Diesel Soot. *Catalysts* **2018**, *8*, 16. [CrossRef]
49. Abboud, J.; Schobing, J.; Legros, G.; Bonnety, J.; Tschamber, V.; Brillard, A.; Leyssens, G.; Lauga, V.; Iojoiu, E.E.; Da Costa, P. Impacts of oxygenated compounds concentration on sooting propensities and soot oxidative reactivity: Application to Diesel and Biodiesel surrogates. *Fuel* **2017**, *197*, 241–253. [CrossRef]
50. Ruitenbeek, M.; van Dillen, A.J.; de Groot, F.M.F.; Wachs, I.E.; Geus, J.W.; Koningsberger, D.C. The structure of vanadium oxide species on γ-alumina; an in situ X-ray absorption study during catalytic oxidation. *Top. Catal.* **2000**, *10*, 241–254. [CrossRef]
51. Golodets, G.I. On Principles of Catalyst Choice for Selective Oxidation. In *Studies in Surface Science and Catalysis*; Centi, G., Trifirò, F., Eds.; Elsevier: Amsterdam, The Netherlands, 1990; Volume 55, pp. 693–700. [CrossRef]
52. Bueno-López, A.; Krishna, K.; Makkee, M.; Moulijn, J.A. Enhanced soot oxidation by lattice oxygen via La^{3+}-doped CeO_2. *J. Catal.* **2005**, *230*, 237–248. [CrossRef]
53. Piumetti, M.; van der Linden, B.; Makkee, M.; Miceli, P.; Fino, D.; Russo, N.; Bensaid, S. Contact dynamics for a solid–solid reaction mediated by gas-phase oxygen: Study on the soot oxidation over ceria-based catalysts. *App. Catal. B* **2016**, *199*, 96–107. [CrossRef]
54. Milt, V.G.; Ulla, M.A.; Miró, E.E. NOx trapping and soot combustion on $BaCoO_{3-y}$ perovskite: LRS and FTIR characterization. *Appl. Catal. B* **2005**, *57*, 13–21. [CrossRef]
55. Khobragade, R.; Kumar Singh, S.; Chandra Shukla, P.; Gupta, T.; Al-Fatesh, A.S.; Kumar Agarwal, A.; Labhasetwar, N.K. Chemical composition of diesel particulate matter and its control. *Catal. Rev. Sci. Eng.* **2019**, *1520*, 5703. [CrossRef]
56. Milt, V.G.; Querini, C.A.; Miró, E.E.; Ulla, M.A. Abatement of Diesel Exhaust Pollutants. NOx Adsorption on Co, Ba, K/CeO_2 Catalysts. *J. Catal.* **2003**, *220*, 424–432. [CrossRef]
57. Sui, L.; Yu, L. Diesel soot oxidation catalyzed by Co-Ba-K catalysts: Evaluation of the performance of the catalysts. *Chem. Eng. J.* **2008**, *142*, 327–330. [CrossRef]

58. Xing, L.; Yang, Y.; Ren, W.; Zhao, D.; Tian, Y.; Ding, T.; Zhang, J.; Zheng, L.; Lia, X. Highly efficient catalytic soot combustion performance of hierarchically meso-macroporous Co_3O_4/CeO_2 nanosheet monolithic catalysts. *Catal. Today* **2020**, *351*, 83–93. [CrossRef]
59. Zheng, C.; Bao, S.; Mao, D.; Xu, Z.; Zheng, S. Insight into phase structure-dependent soot oxidation activity of K/MnO_2 catalyst. *J. Environ. Sci.* **2023**, *126*, 668–682. [CrossRef]
60. Xu, H.; Zeng, L.; Cui, L.; Guo, W.; Gong, C.; Xue, G. In-situ generation of platinum nanoparticles on $LaCoO_3$ matrix for soot oxidation. *J. Rare Earths* **2022**, *40*, 888–896. [CrossRef]
61. Nejar, N.; Makkee, M.; Illán-Gómez, M.J. Catalytic removal of NOx and soot from diesel exhaust: Oxidation behavior of carbon materials used as model soot. *Appl. Catal. B* **2007**, *75*, 11–16. [CrossRef]
62. Fang, J.; Zhang, Q.; Meng, Z.; Luo, Y.; Ou, J.; Du, Y.; Zhang, Z. Effects of ash composition and ash stack heights on soot deposition and oxidation processes in catalytic diesel particulate filter. *J. Energy Inst.* **2020**, *93*, 1942–1950. [CrossRef]
63. Ichiura, H.; Kubota, Y.; Wu, Z.; Tanaka, H. Preparation of zeolite sheets using a papermaking technique Part I dual polymer system for high retention of stock components. *J. Mater. Sci.* **2001**, *36*, 913–917. [CrossRef]
64. Godoy, M.L.; Milt, V.G.; Miró, E.E.; Banús, E.D. Scaling-up of the catalytic stacked wire mesh filters for the abatement of diesel soot. *Catal. Today* **2022**, *394–396*, 434–444. [CrossRef]